Structural optimization of 3D printed designs with spatially-varying material properties

Linda M. Leben

A thesis
submitted in partial fulfillment of the
requirements for the degree of

Masters of Science in Aeronautics & Astronautics

University of Washington

2018

Committee:

Anthony M. Waas

Zelda B. Zabinsky

Program Authorized to Offer Degree:
Aeronautics & Astronautics

University of Washington

Abstract

Structural optimization of 3D printed designs with spatially-varying material properties

Linda M. Leben

Chair of the Supervisory Committee:

Design with conventional, homogeneous materials has historically been limited to finding ideal geometry to fit a given engineering purpose. These designs are driven by necessary geometric discontinuities which cause high strain energy gradients when subjected to mechanical loads, and thus are more likely to fail in these regions. However, new advancements in 3D printing enable manufacturing a solid part with varying material properties; this research seeks to establish techniques for finding optimal designs that use this new technology for the greatest structural benefit. A sequential quadratic programming optimization algorithm was used to find an optimal distribution of Young's modulus that minimize strain energy gradients, as calculated using finite element analysis. This design method has been applied to the case of a thin plate with a circular hole, and has been proven to successfully reduce strain energy gradients and therefore stress concentrations. The resulting optimal design has been 3D printed using applicable technology and the computational model has been validated with experiments. Proposed investigations for future research includes studying the effect of heterogeneous material properties on failure and reliability, and improving applicability to physical systems. Enabling design engineers to customize material properties around geometric discontinuities will provide greater flexibility in reducing stress concentrations without modifying geometry or adding additional mass.

TABLE OF CONTENTS

LIST OF FIGURES

ACKNOWLEDGMENTS

I first thank my thesis advisor, Dr. Anthony Waas, for providing the exciting opportunity to pursue this project and for his constant faith in my abilities. Dr. Waas pushed me beyond what I ever thought possible, and I cannot imagine what my graduate experience would be like without his guidance. I also thank my thesis reviewer, Dr. Zelda Zabinsky for her guidance, interest, and support of my research into optimization algorithms.

Johanna Schwartz is deserving of special thanks as well, for her tireless work 3D printing and testing samples used in this work. Ms. Schwartz's expertise in chemistry and 3D printing technologies was invaluable to this work, as was her patience and mentorship. I also acknowledge the support of the Composite Structures Lab, especially Dr. Royan D'Mello for his guidance during the preliminary stages of this work, and Drew Kang for his research into relevant 3D printing technologies. I am also grateful to Bill Kuykendall for his assistance with tensile testing, and his work ensuring the quality of experiments.

I also thank Dr. Patrick Hammer, for his moral support and advice, and assistance in reviewing my early technical writings on this topic. I could not have succeeded in my studies without encouragement from friends, particularly those in Dayton, OH, who continued to support me from thousands of miles away, and those in Nile Nightmares Haunted House, who welcomed me with open arms. The University of Washington Costume Club, Molly Carton especially, also deserve credit for relieving the stresses of graduate school, even if only for a few hours each week, by listening to worries about my studies in between sewing questions.

Last but certainly not least, I express my sincere and heartfelt thanks to my family; without their love and support throughout my life, this work would not be possible.

DEDICATION

To my parents, Anthony and Karen Leben, for their unending support

Chapter 1
INTRODUCTION

One of the biggest challenges faced by structural engineers is how to design around geometric discontinuities. Designs often require discontinuities such as holes, corners, and notches, and improperly accounting for these factors can be catastrophic, as seen by the de Havilland Comet disasters. The de Havilland Comet was the first commercial jetliner, and unfortunately was met with disaster when two jetliners had in-flight breakups caused by unforeseen stress concentration factors near the rectangular windows [1, 2]. After a detailed investigation by the Federal Aviation Administration, the Comet then was redesigned with stress concentrations in mind, leading to changes in the geometry of the windows and added reinforcements in critical areas [2].

Stress concentrations are now more carefully accounted for, but continue to pose design challenges. Because conventional materials such as metals have homogeneous material properties on a macroscopic scale, the only way to reinforce areas that exhibit high stress concentration is to add more material to reinforce it, or change the geometry. Both of these options may result in undesired deviation from the original intended design. However, the advent of additive manufacturing technologies has given way to new possibilities of design parameters, including the ability to customize designs with different material properties throughout a single part. The purpose of this paper is to explore these opportunities by finding the optimal configuration of material property distribution for a plate with a hole. The implication of this is that future designs can not only be driven by geometry changes, but also by material property distributions, thus possibly improving weight savings.

The design method established in this work may be applicable to additive manufactur-

ing of heterogeneous metals in the future, but advancements in additive manufacturing of polymers already enable variations in material properties. Therefore, this work investigates structural optimization of 3D printed polymers. The vat photopolymerization method developed by Peterson, et al. in particular has been identified for applicability to this study [3]. This 3D printing method involves projecting an image of the desired cross section geometry onto a vat of photoresin; differences in material properties within a single material are achieved by using differences in light intensity.

This study seeks to find the optimal distribution of material properties for a plate with a hole to be 3D printed using vat photopolymerization. For the purposes of this study, a plate with a hole under uniaxial tension was modeled using finite element analysis, and a heterogeneous Young's modulus field was optimized such that strain energy gradients in the part are minimized. Ideally, if gradients in strain energy are absent throughout a volume, the state of stress will be uniform everywhere, with no possibilities for stress concentrations. In this work, stress, strain, and strain energy results from this optimizer were compared to those of a model with uniform Young's modulus. The optimized design was then 3D printed and tested to verify the finite element model and identify any other areas for improvement. Finite element modeling methods and optimization formulations established from this study can be applied to other applicable 3D printing technologies as they become available.

Chapter 2

LITERATURE REVIEW

2.1 3D printing

3D printing is a term for manufacturing processes that create structures by building material in a desired geometry, often in sequential layers, rather than cutting down stock material to the desired shape. Despite recent increased interest in the field, 3D printing is not a new technology; patents for the first 3D printing processes originate from the 1980s. In 1981, Hideo Kodama developed the first 3D printing technology using ultraviolet (UV) hardening photopolymers and a mask blocking out the desired UV exposure area [4]. A few years later in 1984, Chuck Hull submitted a patent on stereolithography, which cures photopolymers in a desired cross-sectional pattern by using UV lasers [5]. Fused Deposition Modeling, or FDM, a process especially common to date that involves extrusion of polymeric filament in the desired cross-sectional pattern of a design, was first developed by S. Scott Crump in 1988 [6].

Several other 3D printing technologies were developed afterwards, but it largely remained an experimental field of research with little industry application until recent years. The expiration of several key patents around 2009-2015 created opportunities for 3D printing manufacturers and researchers, which in turn increased accessibility for educators, hobbyists, and industry [7, 8]. This, coupled with the identification of 3D printing's applicability to more sustainable manufacturing, economic empowerment and efficiency, value as an educational tool, and more has lead to a surge in development of this burgeoning technology [9, 10, 11, 12].

2.1.1 Functionally graded materials

One particular area of interest in 3D printing research is functionally graded materials, that is, solid objects with spatially varying material properties. There are several methods for creating functionally graded 3D printed polymers, including blend melt material extrusion, polyjet, melt material extrusion with nanoparticles, and vat photopolymerization. Blend melt material extrusion is a variation of FDM that uses multiple polymeric materials, blended in different ratios to produce a graded material [13, 14]. Like blend melt material extrusion, polyjet 3D printing is another method that blends polymers in varying ratios, but builds parts using a device similar to a "print head" used in conventional inkjet printing which deposits a layer of liquid polymer and then immediately cures it with UV light [15].

Melt material extrusion with nanoparticles is another variation of FDM that uses the addition of nanoparticles to a polymeric filament to alter the material properties [16, 17, 18]. In a patent filed in 2009, Filisko, et al. outlined a method for mixing graphene nanoparticles into polypropylene pellets to create a stronger nanocomposite filament [16]. Potts, et al. covered further applications and challenges of graphene nanoparticles in more detail in a 2010 review [18].

There is also a variation of digital light processing (DLP) that can produce functionally graded materials, referred to in this work as "vat photopolymerization". In DLP methods, an image of cross section geometry is projected using UV light onto a vat of photopolymer. Since typically this process uses a single, homogeneous material, usually there are not variations in material properties that are desirable for design. However, in 2016, Peterson, et al. found that changes in the light intensity in this process leads to different crosslink densities, and thus, material properties [3]. So, by using a grayscale image of the cross sectional geometry in this process, one can spatially vary the material properties in a desired manner. Since the produced part is still made up of a single material, material properties such as density and Poisson's ratio remain uniform, while only Young's modulus and strength are affected.

2.2 Optimization algorithms

2.2.1 Gradient descent

Gradient descent method is a first order iterative optimization method that seeks a local minimum in a direction proportional to the negative gradient. This algorithm works by choosing an initial guess for the design variables, x_i, and evaluating the objective function and its gradient at that point. Next, the gradient information is then used to find the new point [19]. This process is outlined in Equation 2.1, where $f(x_i)$ is the objective function evaluated at x_i and γ is a small step size value chosen when formulating the model. The sign in front of $g_i * \gamma$ is changed to positive if maximization is desired instead.

$$g_i = \frac{df(x_i)}{dx_i}$$

$$x_{i+1} = x_i - g_i * \gamma \tag{2.1}$$

An advantage of gradient descent is that each iteration is computationally inexpensive; however, for many objective functions the magnitude of the gradient tends to decrease considerably in proximity to a minimum or maximum, which reduces the step size. For some objective functions, this can significantly increase the number of iterations and function evaluations needed to approach the solution. Gradient descent is also limited to continuous and differentiable functions, and is best suited for convex functions. It can only find a local minimum, so for nonconvex functions, its ability to find the global minimum depends on the initial guess.

2.2.2 HASPLID

In order to use an algorithm such as gradient descent on a nonconvex function, it is necessary to modify it such that a global minimum can be found. One such way is to combine it

with an algorithm such as Dynamic Multistart Sequential Search (DMSS), as described in Zabinsky, et al. [20]. DMSS is an implementable algorithm based on Hesitant Adaptive Search with Power-Law Improvement Distribution (HASPLID) theory. This method finds a global minimum by performing a sequence of independent runs with different inital points, restarting whenever a local optimum is reached, which is determined when the number of iterations, k_R, exceeds $n_{Restart}$. The value of $n_{Restart}$ is recalculated for each iteration using Equation 2.2, where subscript R refers to the current run. After the first run, $n_{Restart}$ may be overwritten by the expression shown in Equation 2.3 if it is lower than $n_{Restart}$. At the end of each independent run, ζ is recalculated to solve Equation 2.4, and the probability of failure of reaching the global minimum is estimated using Equation 2.5. The algorithm continues to restart with a new initial guess until it reaches a desired probability of hitting the target solution; stopping the algorithm when p_{Fail} reaches below tolerance parameter δ.

$$T(n,x) = 1 - e^{-x}\sum_{s=0}^{n-1}\frac{x^s}{s!}$$

$$n_{Restart} = k_R\frac{ln(T(j_R+1,-\alpha\zeta ln\epsilon))}{ln(T(j_R,-\alpha\zeta ln\epsilon))} \tag{2.2}$$

$$n'_{Restart} = max(k_1,...,k_{R-1},\sum_{r=1}^{R-1}k_r\frac{ln(T(j_R+1,-\alpha\zeta ln\epsilon))}{ln(p_{Fail})}) \tag{2.3}$$

$$\sum_{r=1}^{R}(j_r-1)+\zeta[R\psi(1+\zeta)-\sum_{r=1}^{R}\psi(k_r+\zeta)]=0 \tag{2.4}$$

$$p_{Fail} = \prod_{r=1}^{R}T(j_r,-\alpha\zeta ln\epsilon) \tag{2.5}$$

The DMSS framework proposed by Zabinsky, et al. performs a stochastic search, that is, each iteration selects values of the design variables based on a chosen distribution [20]. Stochastic search is not dependent on the value or gradient of the objective function, so it

may not necessarily search in the correct direction, nor is it likely for the objective function to strictly improve each iteration. Though DMSS is effective at finding a global minimum, it also requires a high number of function evaluations, and since the runs are independent of each other, the algorithm does not learn from previous runs, so there is potential for redundancy if multiple runs converge to the same local minimum. Because of this, HASPLID with stochastic search may not be appropriate for problems with objective functions that take a long time to evaluate.

2.2.3 Response Surfaces

Another method for solving optimization problems besides iterative methods is known as "meta-modeling." Meta-models create an approximation of the objective function such that the optimization can be performed with fewer or no iterations, significantly reducing run time. One such method of meta-modeling is response surface methodology, in which a set of data is used to find β values from regression statistics that are used to generate an approximation of the objective function [21]. This approximate function often uses a full quadratic model, such as the form shown in Equation 2.6, but other forms such as pure quadratic or linear models may be used as well. This process reduces the computational resources needed to perform the optimization and reduces the need for lengthy iterative processes.

$$RS(x_i) = \beta_o + \sum_{i=1}^{n} \beta_i * x_i + \sum_{i=1}^{n} \sum_{j=i+1}^{n} \beta_{ij} * x_i * x_j + \sum_{i=1}^{n} \beta_{ii} * x_i * x_i \tag{2.6}$$

An advantage of this method is that after an initial set of objective function evaluations, solving for the optimum can be straightforward, and minimal additional function evaluations are needed. However, as the number of design variables increase, the number of β coefficients also increases, which in turn increases the number of inital data points needed. Using a fully quadratic model as expressed in Equation 2.6, the minimum number of data points needed is equivalent to $1 + n + \frac{n(n+1)}{2}$, where n is the number of design variables. This can become

unreasonable as the problem grows; for a model with 100 design variables, 5151 function evaluations are needed to create the response surface, which may outweigh any benefits to the reduced number of iterations needed for this method.

2.2.4 Fmincon

MATLAB's fmincon algorithm is another optimization tool used by engineers. It is a second order optimization algorithm that uses trust-region sequential quadratic programming, a method first suggested by Robert B. Wilson in 1963 [22, 23]. This method is particularly effective for nonlinear convex problems and is suitable for both large and small problems [24, 25]. Trust-region methods involve approximating the objective function with a simpler function within the neighborhood, N, of the current point, x [26]. In essence, trust-region converts a difficult to solve optimization problem of the form shown in Equation 2.7 to the form shown in Equation 2.8, where $f(x)$ is the objective function, x are the design variables, and s is the trial step [24, 26]. Applied to SQP, the simpler approximation is created using the first two terms of the Taylor series representation of the objective function. This then expands the algorithm to the form shown in Equation 2.9, where s is the trial step, H is the Hessian matrix, Ds is a diagonal scaling matrix, and Δ is a positive scalar [26].

$$\begin{aligned} &\min_{x} \ f(x) \\ &\text{s.t. } l \leq x \leq u \end{aligned} \tag{2.7}$$

$$\begin{aligned} &\min_{s} \ q(s) \\ &s \epsilon N \end{aligned} \tag{2.8}$$

$$\begin{aligned} &\min_{s} \ q(s) \\ &q(s) = \tfrac{1}{2} s^T H s + s^T \nabla f \\ &\text{s.t. } ||Ds|| \leq \Delta \end{aligned} \tag{2.9}$$

An approximation of the Hessian of the Lagrangian function is calculated using a quasi-Newton method known as Broyden-Fletcher-Goldfarb-Shanno (BFGS) algorithm to avoid the necessity of calculating a second derivative of the function [26]. The Lagrangian function used in this method is created by first converting any bound constraints to inequality constraints, then combining the objective function with constraints according to Equation 2.10, where $h_i(x)$ are the constraints and λ is an estimate of the Lagrange multipliers. Following BFGS, the Hessian matrix is updated each iteration according to Equation 2.11.

$$L(x, \lambda) = f(x) + \sum_{i=0}^{m} \lambda_i \bullet h_i(x) \tag{2.10}$$

$$\begin{gathered} H_{k+1} = H_k + \frac{q_k q_k^T}{q^T s_k} - \frac{H_k s_k s_k^T H_k^T}{s_k^T H_k s_k} \\ \text{where} \\ s_k = x_{k+1} - x_k \\ q_k = (\nabla f(x_{k+1}) + \textstyle\sum_{i=1}^{m} \lambda_i \bullet \nabla h_i(x_{k+1})) - (\nabla f(x_k) + \textstyle\sum_{i=1}^{m} \lambda_i \bullet \nabla h_i(x_k)) \end{gathered} \tag{2.11}$$

The SQP method used by fmincon has several advantages, including fast convergence even from an infeasible starting point, the ability to use both equality or inequality constraints, and effectiveness for large and small problems, paricularly problems with high nonlinearities [25, 24]. However, this method relies on the Karush-Kuhn-Tucker (KKT) conditions, which guarantee convergence to the optimum only for convex problems, so fmincon may not be best suited for complex, nonconvex problems [24, 27, 28].

Chapter 3
COMPUTATIONAL MODEL

3.1 Finite element model

The goal of this study was to find methods that minimize strain energy gradients caused by geometric discontinuities, so the design method proposed was applied to a simple two dimensional thin plate with a hole loaded in uniaxial tension. A homogeneous plate with a hole is known to have a stress concentration factor of three, and is expected to fail near the hole. An optimized design should be proven to improve the weakness caused by the geometric discontinuity, which can be specifically observed in two ways: exhibit a lower stress concentration factor than three, and fail in a region away from the hole.

This two-dimensional plane stress problem was modeled assuming linear elasticity using a previously established finite element code [29]. The length of the plate is twice as large as the width of the full plate, and the diameter of the hole is one fifth of the width. Problem setup can be seen in Figure 3.1; the plate is fixed in the x-direction on the left edge and fixed in the y-direction on the bottom edge. By assuming symmetry, only the top half of the plate is modeled to reduce computational cost. A small prescribed displacement is applied to the right edge.

3.2 Optimization model

3.2.1 Design variables

Since the goal of this project was to find the best spatially varying Young's modulus throughout the part, each element had a different elastic stiffness matrix, which was calculated using

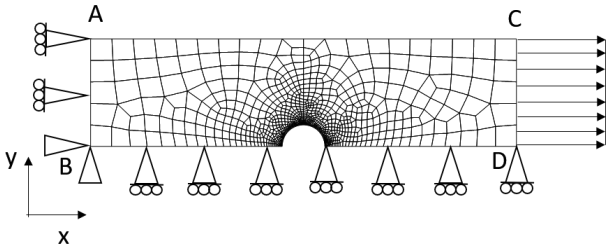

Figure 3.1: Free body diagram of model used in this work.

the plane stress-strain relation, as shown in Equation 3.1.

$$\begin{pmatrix} \sigma_x \\ \sigma_y \\ \mathcal{T}_{xy} \end{pmatrix} = \frac{E}{1-\nu^2} \begin{bmatrix} 1 & \nu & 0 \\ \nu & 1 & 0 \\ 0 & 0 & \frac{1-\nu}{2} \end{bmatrix} \begin{pmatrix} \epsilon_x \\ \epsilon_y \\ \gamma_{xy} \end{pmatrix} \tag{3.1}$$

To reduce the computational cost of optimizing Young's modulus, design variables were defined at control points generated based on geometry rather than optimized for every element. Selection of control point locations can be seen in Figure 3.2. The values at these points were linearly interpolated to the center of each element to obtain Young's modulus values for each element, which were used for finite element calculations, as well as calculation of the objective function. Based on the value of the objective function, the solver then chose new guesses for Young's modulus at the control points, and interpolation and finite element calculations were repeated for each iteration. This process lowered the number of design variables from thousands (3109 in the mesh shown) to about 115, which reduces run time on a high performance computer using 16 processors from several weeks or more to only a few days. An additional benefit of controlling Young's modulus in this manner is that it ensures a more continuous distribution of material properties throughout the part.

Young's modulus was constrained to the maximum and minimum values possible for a given material. Poisson's ratio and density were fixed values throughout the part; this is

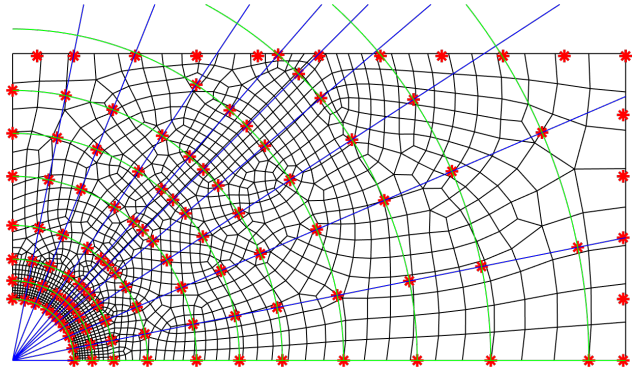

Figure 3.2: Location of control points at which Young's modulus was optimized.

sufficient for modeling materials used in vat photopolymerization, as neither Poisson's ratio nor density are altered by light intensity.

3.2.2 Objective function

The goal of the optimizer was to minimize strain energy gradients in the plate, so strain energy at each Gauss point was calculated with the stress and strain values at each Gauss point using Equation 3.2. A linear interpolation function was then used to generate a function of strain energy in terms of x and y. The spatial gradient of strain energy across the center of each element was then calculated using Equations 3.3 and 3.4, where (x, y) are the coordinates of the center of the element, and dx and dy are small distances within the element, a value which is the same for every element and was chosen as about one quarter of the length of the smallest element in the mesh. The magnitude of the gradient was then calculated using Equation 3.5, and the objective function value, G, was calculated using Equation 3.6. The optimization algorithm worked to find a value of Young's modulus at each of the control points that minimized this value of G, as stated in Equation 3.7.

$$W = \frac{1}{2}\sigma_{ij}\epsilon_{ij} \tag{3.2}$$

$$\nabla W_x^e = \frac{W(x+dx,y) - W(x,y)}{dx} \tag{3.3}$$

$$\nabla W_y^e = \frac{W(x,y+dy) - W(x,y)}{dy} \tag{3.4}$$

$$||\nabla W^e|| = \sqrt{(\nabla W_x^e)^2 + (\nabla W_y^e)^2} \tag{3.5}$$

$$G = \max ||\nabla W^e|| \tag{3.6}$$

$$\begin{aligned} &\min_E \ G(E) \\ &\text{s.t. } E_{min} \leq E \leq E_{max} \end{aligned} \tag{3.7}$$

3.3 Optimization algorithm

The structural optimization problem at hand is complex for two reasons: the convexity of the problem is unknown, and each function evaluation requires a full finite element analysis evaluation. This makes it desirable to find an algorithm that can both confidently find a global min of a nonconvex problem, and can do so in as few iterations or function evaluations as possible. The following section outlines studies into selected optimization algorithms and selection of an appropriate algorithm.

3.3.1 HASPLID with gradient descent

As previously indicated in Chapter II, gradient descent can be an efficient means of optimizing a convex problem, but is not effective for more complex non-convex problems. HASPLID, on the other hand, is an effective method of optimizing non-convex problems, but is not efficient when used with stochastic search. Therefore, an algorithm combining HASPLID with

gradient search was investigated. Implementation was straightforward, the DMSS framework proposed by Zabinsky, et al. was used, except each iteration selected values of design variables using gradient descent rather than a stochastic distribution [20].

In order to test the effectiveness of an algorithm combining gradient descent with HASPLID, it was used to solved the Ackley function in two dimensions, shown in Equation 3.8 and Figure 3.3 [30, 31]. The Ackley function was chosen because it is continuous and differentiable, and has several local minimum as well as one global minimum at $f(0,0) = 0$. This function was solved in two dimensions for visualization purposes, but can be easily modified for higher dimensions as well.

To implement the Ackley function, the derivative was found with respect to each design variable, Equation 3.9, and the design variables were constrained to between -5 and 5 in each dimension. Parameter values were chosen to be $\alpha = 1.00$, $\delta = 0.01$, $\epsilon = 0.01$, $\gamma = 0.05$, and ζ initialized at 1.00.

$$f(x,y) = -20e^{0.2\sqrt{0.5(x^2+y^2)}} - e^{0.5(cos(2\pi x)+cos(2\pi y))} + e + 20 \tag{3.8}$$

$$\begin{aligned} g_x(x,y) = \frac{df}{dx} &= \frac{x4\sqrt{0.5}e^{-0.2\sqrt{0.5(x^2+y^2)}}}{\sqrt{x^2+y^2}} + \pi sin(2\pi x)e^{0.5(cos(2\pi x)+cos(2\pi y))} \\ g_y(x,y) = \frac{df}{dy} &= \frac{y4\sqrt{0.5}e^{-0.2\sqrt{0.5(x^2+y^2)}}}{\sqrt{x^2+y^2}} + \pi sin(2\pi y)e^{0.5(cos(2\pi x)+cos(2\pi y))} \end{aligned} \tag{3.9}$$

The results of four trials solving the Ackley function using this algorithm are presented in Table 3.1 and visualized in Figure 3.4. In Figure 3.4, green stars represent the global minimum found, red circles indicate the initial values of independent runs, and black x's represent iterations within runs. Within each run, the algorithm iterates towards a local minimum in the opposite direction of the gradient. Restarting at different values does produce better results than any individual run, but of the four successful trials shown in Figure 3.4, only two reached the minimum in both dimensions. The other two trials reached a minimum in one dimension but not the other.

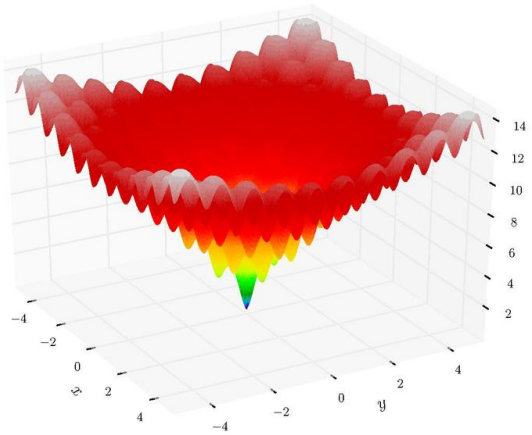

Figure 3.3: Ackley function in two dimensions.

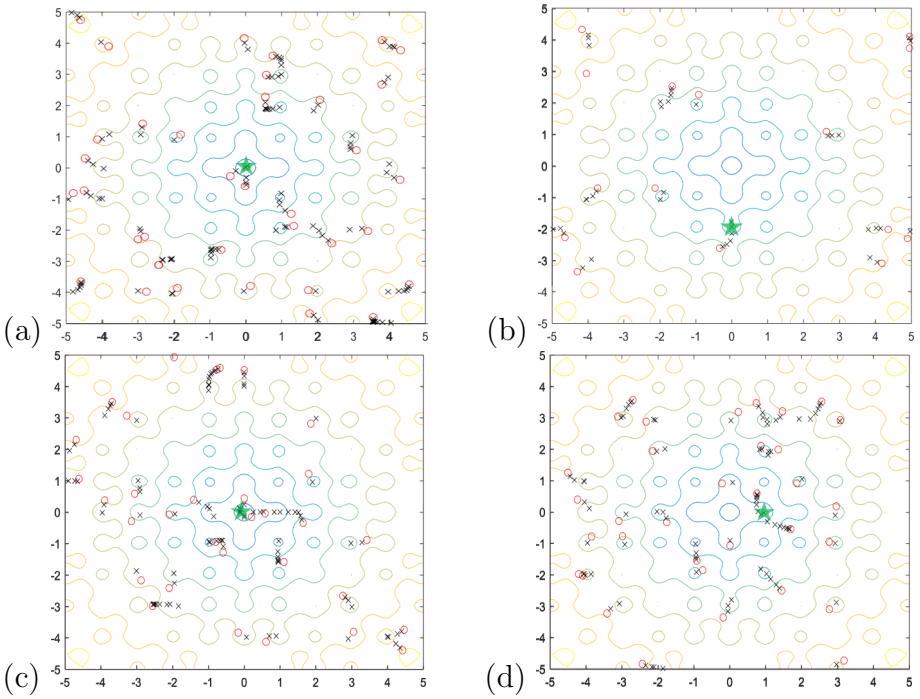

Figure 3.4: Results of gradient search optimization with multi-start.

Table 3.1: Optimum solutions found for gradient search with multi-start.

Trial	x	y	f(x,y)
a	-0.004	0.009	0.0275
b	0.0061	-1.19	4.93
c	-0.098	-0.0019	0.5141
d	0.956	0.0249	2.5973

Though some tests of the algorithm completed successfully, failures were also common. For several trials, a ζ value that solved Equation 2.4 could not be found, or the algorithm continued running indefinitely. The reason for these failures stems from the nature of Equation 2.4. As stated by Zabinsky, et al., "the expression decreases monotonically from the nonnegative value of $\sum_{r=1}^{R}(j_r - 1)$ at $\zeta = 0$ to the nonpositive value of $\sum_{r=1}^{R}(j_r - k_r)$ at $\zeta = +\infty$," so finding a root of Equation 2.4 should be possible [20]. However, if $j_r = k_r$, the lower limit approaches zero, never reaching a negative value, thus making finding a root impossible. As a result, the algorithm may incorrectly set ζ as a large value that will result in p_{Fail} always being equal to one, indicating that the global minimum has not been found.

Put more simply, if every iteration is a record, then the algorithm will either fail to find a ζ value or will do so incorrectly and will never know if the minimum has been reached. DMSS was designed with stochastic search in mind, in which every iteration being a record would be fairly uncommon. In the case of gradient search, it is common, even expected, for almost every iteration to be a record. As a work around for the purposes of this study, a fairly large value of $\gamma = 0.05$ was used so that the minimum was occasionally overshot, thus causing $j_r \neq k_r$, which allowed an accurate ζ and p_{Fail} to be found. This is not an ideal solution, however, as many trials still failed and the large γ may have caused insufficient convergence on the global minimum.

One solution to this is to only count an iteration as a record if it improves the current record by at least some buffer value. This way, if the function either reaches a plateau or is sufficiently close to an optimum already, j_r does not increment but the simulation is allowed to continue to run. With this modification, problems with solving for ζ are avoided by ensuring $j_r < k_r$, and all HASPLID theory is still valid. Using a sequence of independent runs does work well with gradient descent, but HASPLID formulations implemented in this study are not recommended without careful modification.

3.3.2 HASPLID applied to finite element model

Because HASPLID with gradient search can be an effective means of finding a global optimum, it was investigated for application to this problem. However, one of the limitations of gradient descent is that it requires the objective function to be differentiable with respect to the design variables. The finite element model in this case is differentiable with respect to Young's modulus at the elements, but is not easily differentiable with respect to Young's modulus at control points. An alternative to differentiation of the objective function is using finite differences, however, this requires the objective function to be evaluated an extra $2n$ times *per iteration*, where n is the number of design variables. This quickly becomes unreasonable for large problems, and is therefore undesirable for this problem with 115 design variables.

An alternative to gradient descent with multi-start is to use a stochastic search method instead, such as hit and run. Hit and run searches in a random direction in n space and does not require evaluation of the gradient of the function [32]. Hit and run generates new points for each iteration using Equation 3.10, where k refers to the iteration number, x is the value of the design variable, λ is a real scalar, and D_k is a random direction. D can be generated using hyperspherical directions, which generates points d_i according to a normal distribution, and then is normalized into a unit vector, as shown in Equation 3.11. There are

other methods for determining direction sets, such as coordinate direction, which is covered in more detail in "Stochastic Adaptive Search for Global Optimization" by Zelda Zabinsky [32].

$$x_{k+1} = x_k + \lambda D_k \tag{3.10}$$

$$D = (d_1, d_2, d_3, ...d_n)(\sum_{i=1}^{n} d_i^2)^{-1/2} \tag{3.11}$$

Hit and run is well suited for HASPLID as it is rare for each iteration to be a record, however, this also means that it does not search in the most efficient direction towards a local minimum as gradient descent does. This increases the computational cost, but for purposes of this project, hit and run with multi-start was investigated in order to avoid the complications of gradient descent applied to this problem.

3.3.3 Benchmarking

In order to perform an initial check on the potential of these algorithms, a low resolution model was used, with fewer elements (995) and control points (17), which reduces the run time of finite element calculations and lowers the number of design variables. This low fidelity model, shown in Figure 3.5, will not provide a good resolution on the desired design, but is sufficient for an initial study of the efficacy of global optimization algorithms.

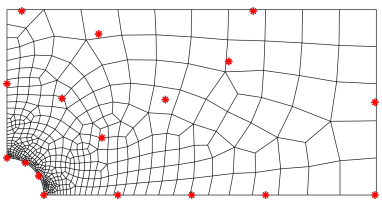

Figure 3.5: Low fidelity model used for this study.

Table 3.2: Data from algorithm benchmarking study.

	Response Surface	Multi-start	fmincon (uniform IC)	fmincon (random IC)
value of objective	10.6	9.15	1.22	1.23
function	10.6	5.15	1.23	1.23
	9.6	6.77	1.22	1.23
number of	303	300	4511	4219
function	312	1689	4511	4474
evaluations	313	474	4511	3707
runtime (min)	8	8	125	112
	7	48	126	119
	9	14	126	100

Multi-start with hit and run, Response Surface, and fmincon were each run three times to test the fidelity and consistency of the solutions as well as compare computational resources needed. Because convexity of the problem is unknown and fmincon does not guarantee convergence for nonconvex problems, fmincon was tested both for a uniform and randomized initial conditions. Quantitative results on the results and performance of the algorithms is shown in Table 3.2, and qualitative results on the Young's modulus configuration found by each algorithm can be observed in Figure 3.9.

Response Surface consistently required fewer function evaluations, and ran very quickly, each trial completing in less than 10 min. However, it performed worse at minimizing the objective function than the other two algorithms. Furthermore, the configurations that were found were inconsistent from each other. Solutions were also found outside of the feasible region and adjusted back to the constraints, therefore the results shown may not actually

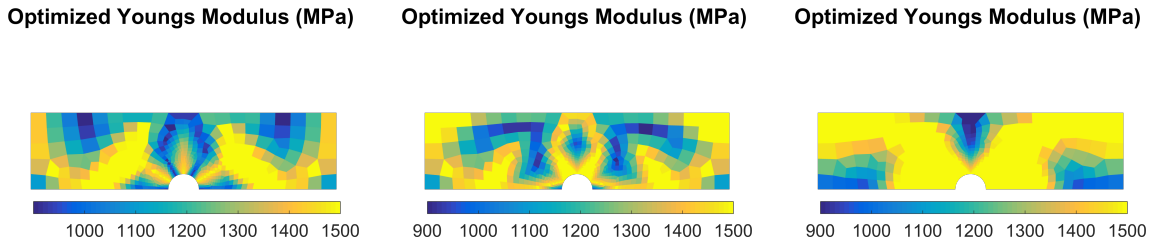

Figure 3.6: Optimal Young's modulus solution found for three trials using Response Surface.

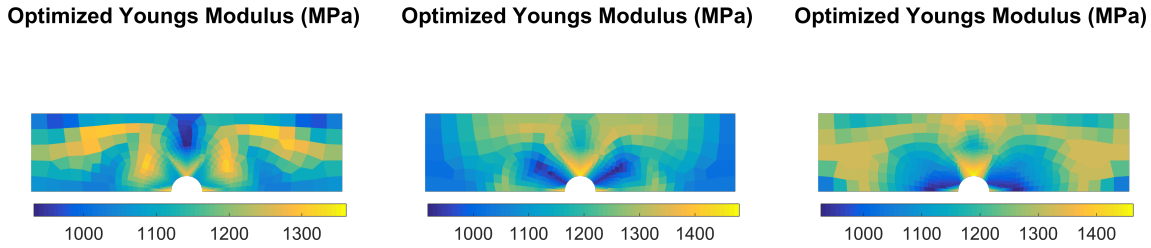

Figure 3.7: Optimal Young's modulus solution found for three trials using multi-start.

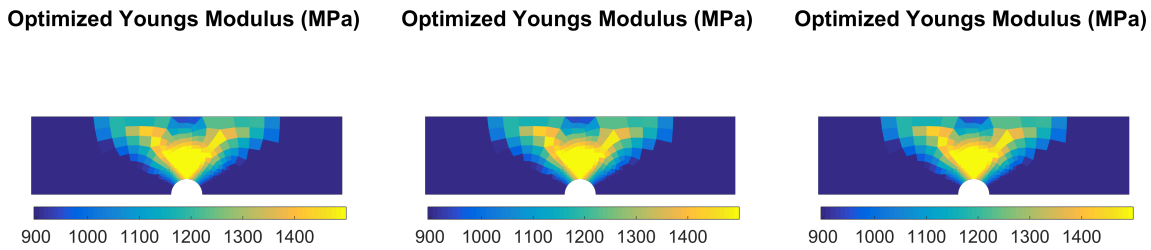

Figure 3.8: Optimal Young's modulus solution found for three trials using fmincon with uniform initial conditions.

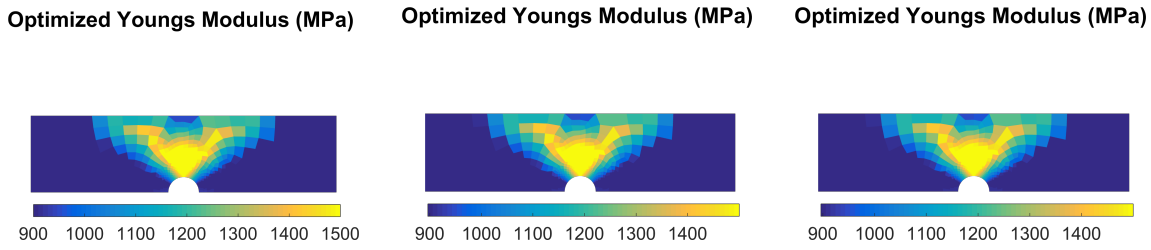

Figure 3.9: Optimal Young's modulus solution found for three trials using fmincon with randomized initial conditions.

represent the optimum within the feasible region. In conclusion, though Response Surface methodology is computationally inexpensive, it is ill-suited for this problem.

Multi-start with hit and run was able to minimize the objective function better than Response Surface. Computational expenses needed vary widely; though multi-start is able to find a global minimum, because each run is independent of other runs, how quickly it is able to find the optimum depends on how soon it selects an initial guess close to the optimum. Overall, multi-start tends to require a greater number of function evaluations, and thus, computational time than required for Response Surface. Qualitatively, the configurations found by multi-start vary from each other, but some similar patterns appear to be evident. This suggests that further adjustment of HASPLID parameters, or improvement of the distributions used in hit and run and in initialization may improve performance.

The SQP algorithm used by fmincon was able to minimize the objective function best out of the algorithms tested. It required more function evaluations and a greater run time than the other algorithms, but its performance was consistent across each trial. Furthermore, the configurations found by this algorithm were consistent with each other, even for different, randomized initial conditions. Of particular interest is that the same solution was found for the different initial conditions, which indicates that the objective function is likely convex in the feasible region. Despite the additional computational expense needed, because of the quality and consistency of solutions found with this algorithm, it is clear that it is best suited for this problem of the algorithms investigated. The computational expense will significantly increase for a refined mesh and more design variables, however, parallel processing can make this expense more reasonable.

Chapter 4
MANUFACTURING WITH VAT PHOTOPOLYMERIZATION

Of the 3D printing methods outlined in Chapter II, vat photopolymerization was determined to be best suited for this application. Because vat photopolymerization spatially varies crosslink density within the same polymer, it allows for studying the effects of changing only Young's modulus and strength, keeping other material properties such as density constant. Furthermore, the technology and equipment were readily available, as well as the potential to collaborate directly with the researchers who developed the process, thus allowing for consistency from the Peterson study [3].

4.1 3D printer setup

Objects were printed using a SeeMeCNC Droplit vat photopolymerization printer in conjunction with an Acer P1500 projector with the brightness decreased to 25%, setup can be seen in Figure 4.1. The printing method, printer modifications, and print parameters are the same as those previously reported by Peterson, et al. [3]. The z-lift distance was modified to be 3 mm, and all other print parameters were kept the same. Printed samples were wiped with ethanol to remove residue from the surface, and air-dried.

All vat photopolymerization additive manufacturing was done using the same printer and projector settings, and average light intensities. As such, the digital grayscale image correlates to the same outputted light intensity as the work done by Peterson, et al., and thereby the same outputted Young's modulus [3]. An optimized plate design can be printed using this method by generating an image of the desired Young's modulus configuration and converting it to a grayscale image. The optimized grayscale image design was generated

with the lowest Young's modulus corresponding to 70% gray, and the highest corresponding to 100% gray. In this printing setup, these values correlate to a maximum projector light intensity of 80 klx and 200 klx, respectively, with a linear correlation between light intensity and Young's modulus and strength. Findings from Peterson, et al. suggest that grayscale values outside this range for this specific printer and photoresin setup yield significant defects, printing failure, or no longer yield changes in crosslink density [3].

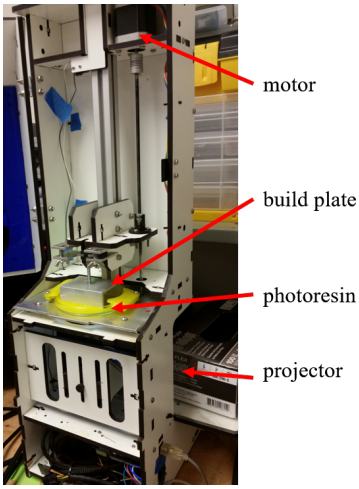

Figure 4.1: Vat photopolymerization 3D printer setup.

Due to the size of the build plate and photoresin vat, printable designs for this set up are limited to fitting in the 8 cm diameter vat, with maximum thickness of about 3 mm and with printing failure occurring more frequently with increased thickness.

4.2 Material

MakerJuice G+ Yellow photoresin was used to manufacture samples; this material can achieve Young's modulus ranging $0.9 < E < 1.5$ GPa, and has Poisson's ratio of 0.3 and density of 1.1 g/cm^3 [33]. The resin is sensitive to humidity and temperature variations, so a controlled environment was used to ensure print quality and reduce the frequency of failed

prints. Photoresins polymerize and change crosslink density when exposed to UV light, so printed samples and parts were protected from sunlight to prevent undesired material property changes.

Chapter 5

FINITE ELEMENT ANALYSIS RESULTS

5.1 Model verification

In order to test the finite element model, three different meshes were generated for a mesh refinement study, shown in Figure 5.1. Optimized Young's modulus results for the three meshes can be seen in Figure 5.2. Due to the heterogeneous nature of the design, nonconventional mesh refinement was required. In this specific design, Young's modulus exhibits high gradients from high to low values in a "V" shape domain radiating out from the hole, so the mesh needed to be refined in those areas in order to better capture the results, and this was implemented in the mesh seen in Figure 5.1c. However, mesh refinement is problem dependent and requires an iterative process for other geometries or loads. Across all meshes tested, a similar pattern was seen for each mesh, so it was reasonable to conclude that the model was fairly robust. The mesh shown in Figure 5.1c showed the best refinement of the solution, and thus was used for all calculations going forward.

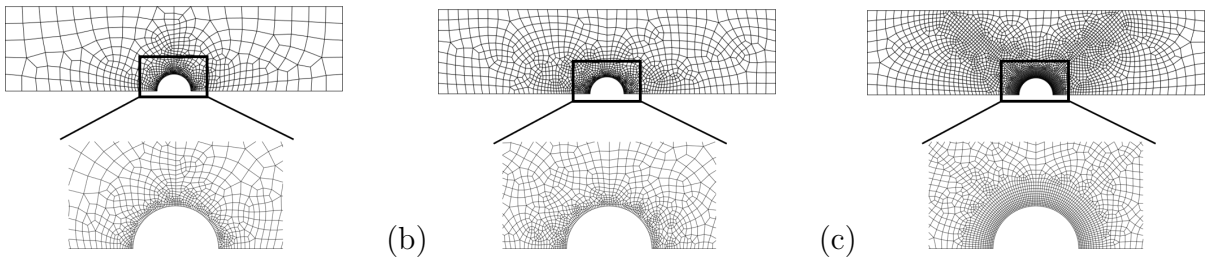

Figure 5.1: Meshes used in refinement study with increasing refinement from (a) to (c).

Due to limitations with the SQP algorithm used by fmincon, it was necessary to check

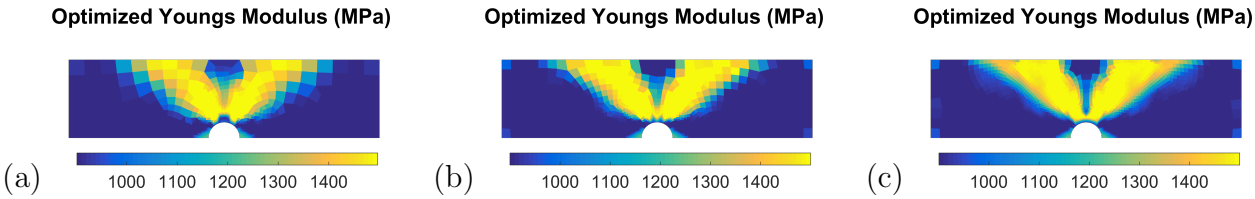

Figure 5.2: Optimized Young's modulus field for each mesh.

different initial guesses in order to further verify convexity of the problem in the feasible region. Three different initial guesses of Young's modulus fields were tested: two randomly generated and one uniform. Plots of these guesses and their corresponding solutions can be seen in Figure 5.3. The solutions were qualitatively similar regardless of initial guess, which further verifies the convexity of this problem. Going forward, a uniform initial guess was used and the design shown in Figure 5.3e was chosen as the optimal design used in experiments.

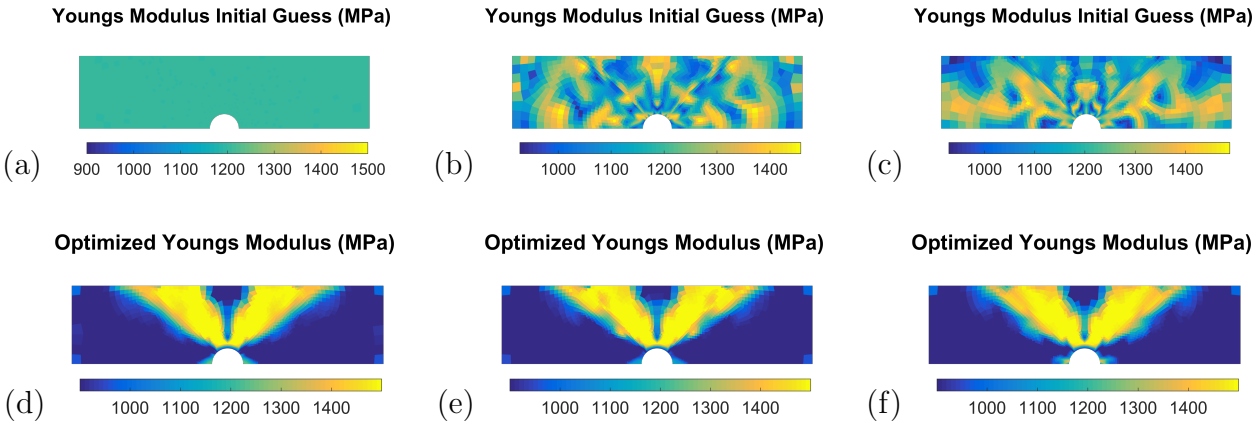

Figure 5.3: (a-c) Initial guesses tested and (d-f) corresponding Young's modulus solutions.

5.2 Analysis of optimal design for vat photopolymerization

An optimal configuration for a plate with a hole constrained to a material that can achieve Young's modulus ranging $0.9 < E < 1.5$ GPa was found, and has been confirmed to reduce

peak stress and yield more uniform stress and strain fields when subjected to uniaxial tension. Both stress and strain exhibit less dramatic gradients as compared to homogeneous Young's modulus, as shown in Figures 5.4 and 5.5. Note that because of the difference in peak values, field output results were plotted on different scales in order to visualize changes in gradient distribution. Peak values of both stress and strain are approximately 40% lower than that of a homogeneous plate. In addition, stress and strain are less localized and more evenly distributed in the plate.

Also of interest is the fact that stress and strain fields do not appear similar as is expected for homogeneous plates; this is because changes in Young's modulus result in different stress-strain relations for each element. The objective function was based on strain energy gradients, which is calculated using both stress and strain, so this discrepancy in distribution would not have affected optimization calculations. Strain energy results are shown in Figure 5.6, which also demonstrate a reduction in gradients, as was the goal of the optimization.

In order to make a qualitative comparison regarding the improvement in gradients, stress factor and strain energy were both normalized using values in the far field of the plate away from the hole. Values for normalized stress factor and strain energy along the centerline from the edge of the hole to the edge of the plate are plotted in Figure 5.7. This does not capture the full effect of the change of gradients since stress concentrations are distributed differently from that of a homogeneous plate, but it does show that the stress concentration factor has been reduced from 3.10 to about 1.89 and that the location of the peak value has shifted inwards from the edge of the plate. This, combined with qualitative observation of the field output data, supports the conclusion that selectively changing Young's modulus to that of the optimized configuration significantly reduces gradients, thus reducing the structural impact of the hole.

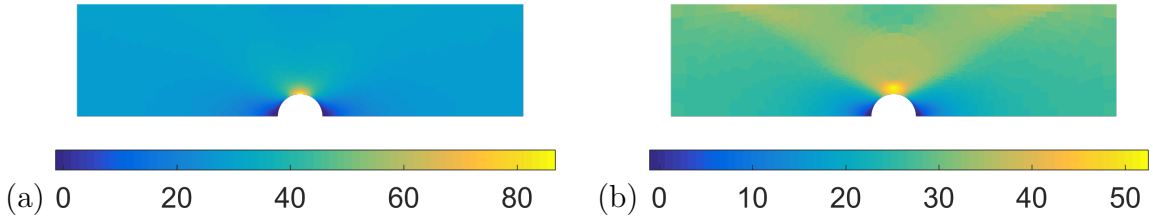

Figure 5.4: Stress, σ_x (MPa), results for (a) homogeneous and (b) optimized plate designs.

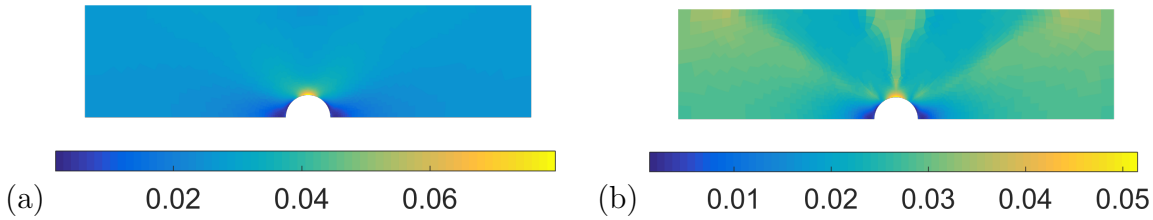

Figure 5.5: Strain, ϵ_x (mm/mm), results for (a) homogeneous and (b) optimized plate designs.

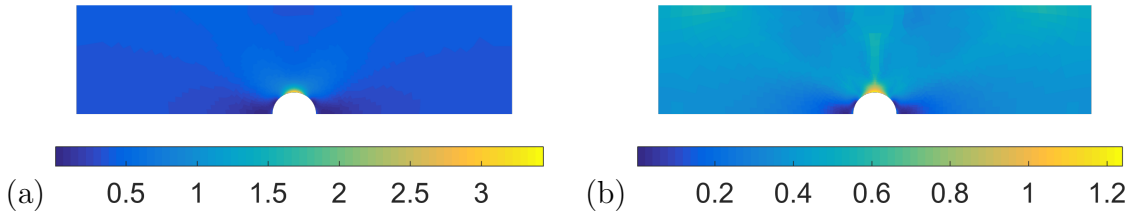

Figure 5.6: Stain Energy, W (MPa), results for (a) homogeneous and (b) optimized plate designs.

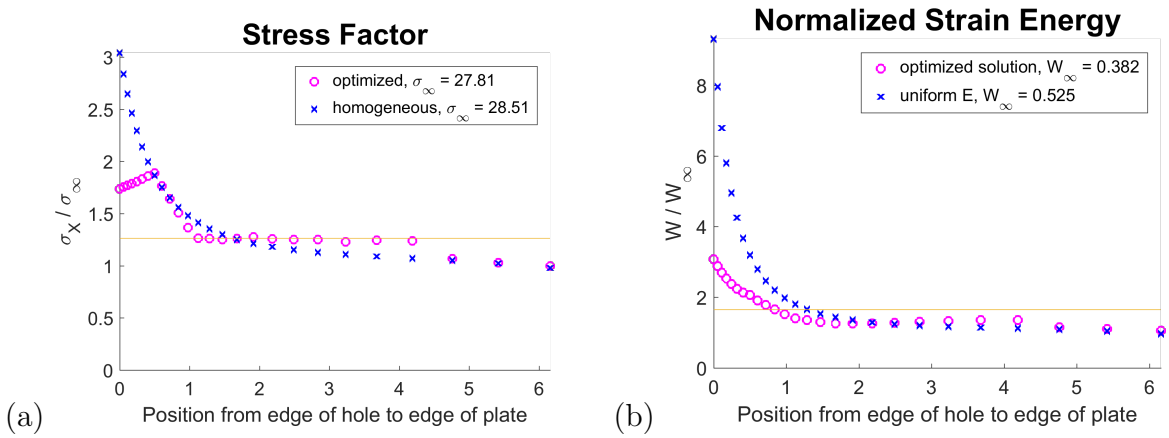

Figure 5.7: (a) Stress Factor and (b) Normalized Strain Energy along centerline from edge of hole to edge of plate.

5.3 Theoretical unconstrained design

In the design found for a plate that can be produced using the selected material, Young's modulus values reach material constraints in some regions, therefore it is reasonable to assume that a larger feasible region may lead to even further reductions in stress concentrations. Therefore, it is of interest to study the theoretical solution for an unconstrained material. That is, if one could print a solid part with any Young's modulus range, what would the design look like? To find the solution to this question, the optimization solver was run with Young's modulus constrained to only positive values, $0 < E < \infty$. Results for the unconstrained solution can be seen in Figure 5.8.

In the case of the unconstrained plate, the stress concentrations were further reduced to a maximum value of 1.63, and peak value located further from the edge of the hole, as can be see in Figure 5.9. The solution suggests that an optimal plate would have a minimum Young's modulus of zero, which is a nonphysical result. However, it does imply that an "ideal" material for a design that minimizes strain energy gradients should be able to achieve as low of a value for Young's modulus as possible. Despite the nonphysical nature

of this design, the most interesting aspect of this solution is that even for an unconstrained problem, a similar "V" configuration is found for the Young's modulus field. These results imply that in general, a plate with hole loaded in tension should be reinforced to have greater stiffness in those regions. The specific values for the material properties are dependent on the capabilities of the material to be used.

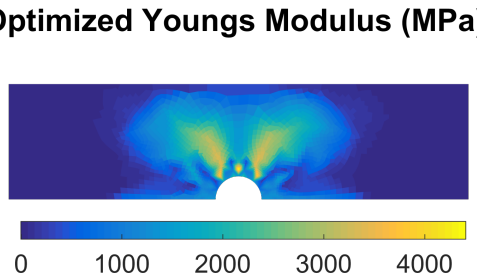

Figure 5.8: Optimized Young's modulus for unconstrained plate with hole.

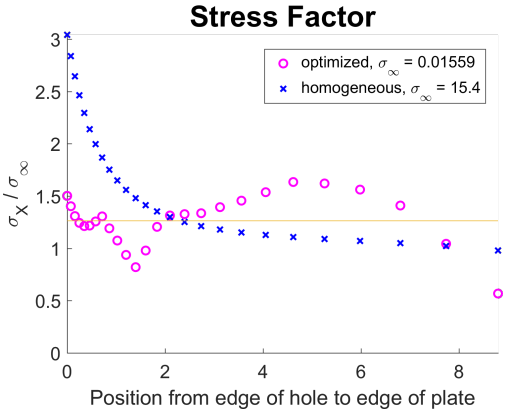

Figure 5.9: Stress Factor along centerline from edge of hole to edge of plate. Optimized results are for unconstrained plate.

Chapter 6

EXPERIMENTS

6.1 Dogbone experiments

Peterson, et al. have proven a linear relationship between light intensity and material properties, and have gathered compression data, but tension data was not yet available [3]. In order to obtain tension data, dogbone specimens were printed according to ASTM D638 Type V at different light intensities, and were tensile tested to verify Young's modulus and tensile strength [34]. Tensile testing was done using an Instron 5585H load frame with a 2 kN load cell controlled by Bluehill 3.0 software. Elongation was done at a rate of 1 mm/min and strain data on dogbone specimens was collected via a video extensometer. This data was then post processed using specimen geometry to generate stress-strain curves which provide Young's modulus and tensile yield strength, shown in Figure 6.1. As expected, since the photoresin is linearly elastic, Young's modulus was unchanged from data collected by Peterson, et al [3]. Because the material is brittle, tensile strength was lower than compression strength, but should still exhibit a linear relationship with light intensity. Two percent offset yield strength was found to range from about 7 to 12 MPa; this strength data will be used in future studies evaluating the effect of the heterogeneous design on failure.

6.2 Optimal and homogeneous plates

In order to verify computational results, optimized and homogeneous plate designs were tensile tested as well. It was necessary to find an equivalent homogeneous plate to adequately compare results of the optimized design. In order to do so, reaction forces and applied displacement in the finite element model at the loaded edges were used to find macroscopic

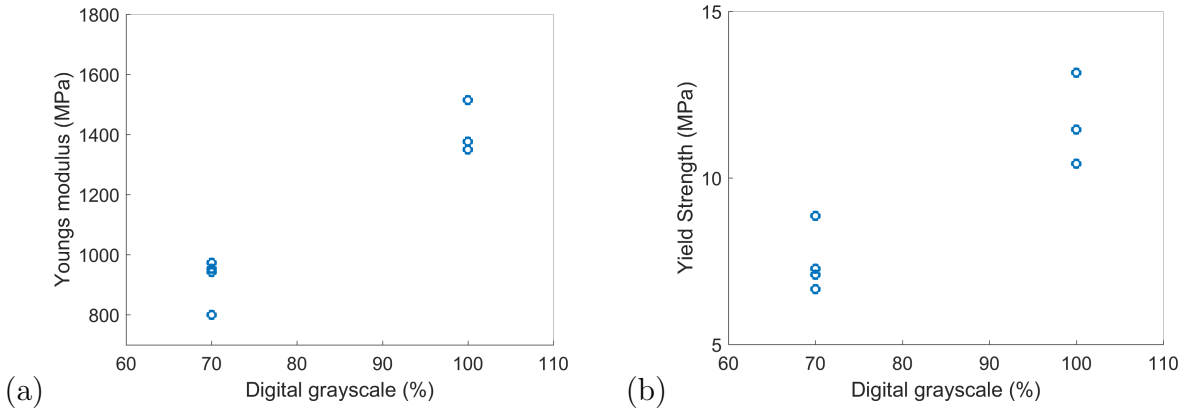

Figure 6.1: (a) Relationship between digital grayscale value used in vat photopolymerization and Young's modulus. (b) Relationship between grayscale value and tensile yield strength.

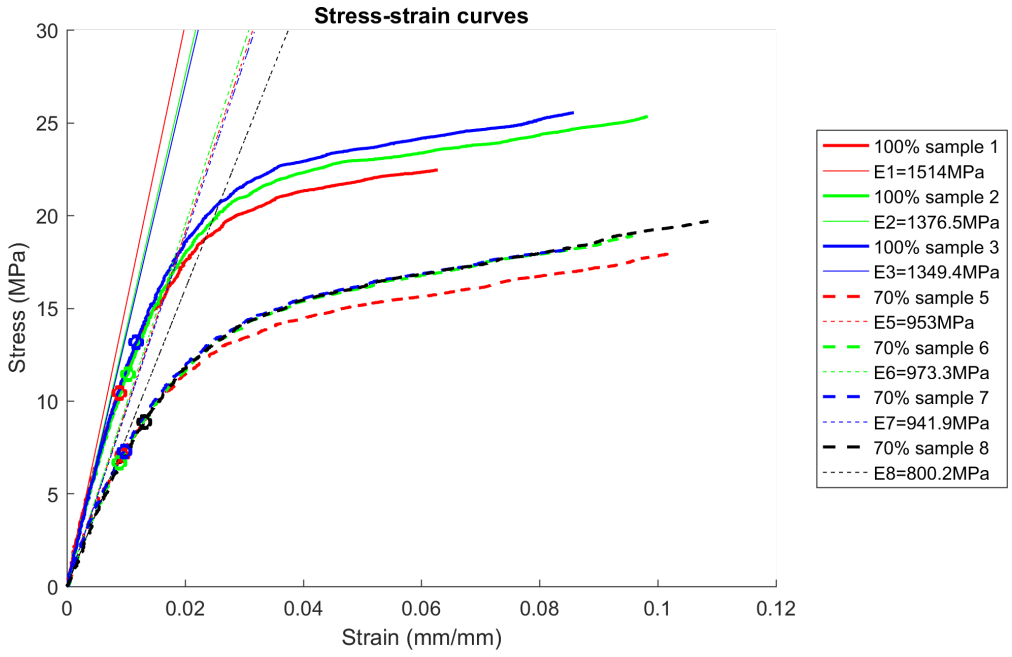

Figure 6.2: Stress-strain plots for dogbone samples tested. Solid lines correspond to data of samples printed at 100% digital grayscale, and dashed represents those printed at 70%.

stress and macroscopic strain using Equations 6.1 and 6.2, where L was the total length of the plate, δL was applied displacement, A was the cross sectional area of the plate, and F was the sum of the reaction forces on the left edge of the plate obtained from the finite element solution. These stress and strain values were used to calculate an "effective" global stiffness of the optimized plate by the stress-strain relation, Equation 6.3, where $\hat{E}$ is "effective" global stiffness. This process was repeated for homogeneous plates of 0.9 GPa and 1.5 GPa, and linear interpolation was used to find the Young's modulus of a homogeneous plate that yielded the same "effective" global stiffness as the optimized design, as seen in Figure 6.2. This evaluation, combined with calibration done by Peterson, et al. determined that a homogenous plate with a hole printed using 77.6% gray would be comparable to the global stiffness of the optimized design.

$$\hat{\sigma} = F/A \tag{6.1}$$

$$\hat{\epsilon} = \delta L/L \tag{6.2}$$

$$\hat{\sigma} = \hat{E}\hat{\epsilon} \tag{6.3}$$

Grayscale images were then generated of both homogeneous and optimized designs; the homogeneous plate image having a uniform digital grayscale value of 77.6%, and the optimized plate image was generated using an image of the Young's modulus design and converting it to grayscale, with the lowest Young's modulus corresponding to 70% gray, and the highest corresponding to 100% gray, as shown in Figure 6.4. Geometric ratios were kept consistent from finite element model, scaled to printer setup, dimensions shown in Figure 6.5. All 3D printed plates yielded relatively consistent dimensions. Measurements of homogeneous plate had a coefficient of variation of 2.87% for the thickness, 0.164% for width, and 0.096% for length. Measurements of optimized plate had a coefficient of variation of 7.54%

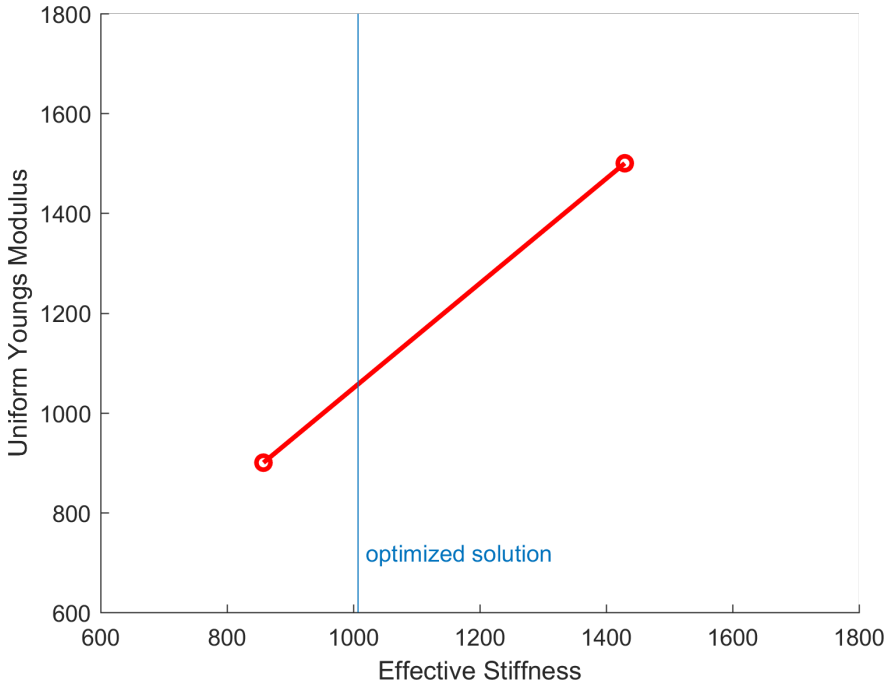

Figure 6.3: Graphical visualization of method used to find equivalent homogeneous design.

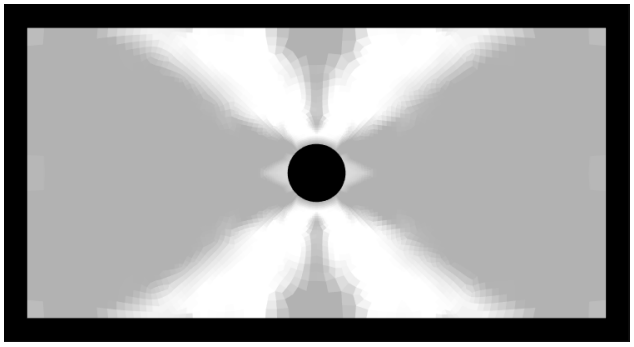

Figure 6.4: Grayscale image used in vat photopolymerization process.

for thickness, 0.661% for width, and 0.107% for length. Differences in thickness were more noticeable, this was due to challenges associated with manufacturing such a thin sample using this method of 3D printing, and would improve for a thicker plate.

Additionally, optimized plates exhibited somewhat higher variation in geometry. This was expected since lower light intensities have been shown to yield smaller geometry than desired [3]. The relationship between geometry changes and light intensity is linear, but geometry dependent; lower light intensities correlate to smaller printed dimensions than desired design. For this particular geometry the effects appear minimal, the largest noticeable variation is that for optimized plates, the edge width at the centerline of the object in line with the hole was consistently about 1.1% narrower than the rest of the plate, this small geometry difference can be seen in Figure 6.6. As shown by Peterson, et al., it is possible to counteract this effect by applying geometry adjustments where necessary to grayscale images [3]. Future work may include applying this method to this design.

Tensile tests of optimized and homogeneous plates were performed using the same equipment and setup as dogbone specimens. Strain distribution fields of the plates during deformation were captured using Digital Image Correlation (DIC); strain fields just before failure, as captured by DIC, can be seen in Figure 6.6. The optimized plate exhibits a more evenly

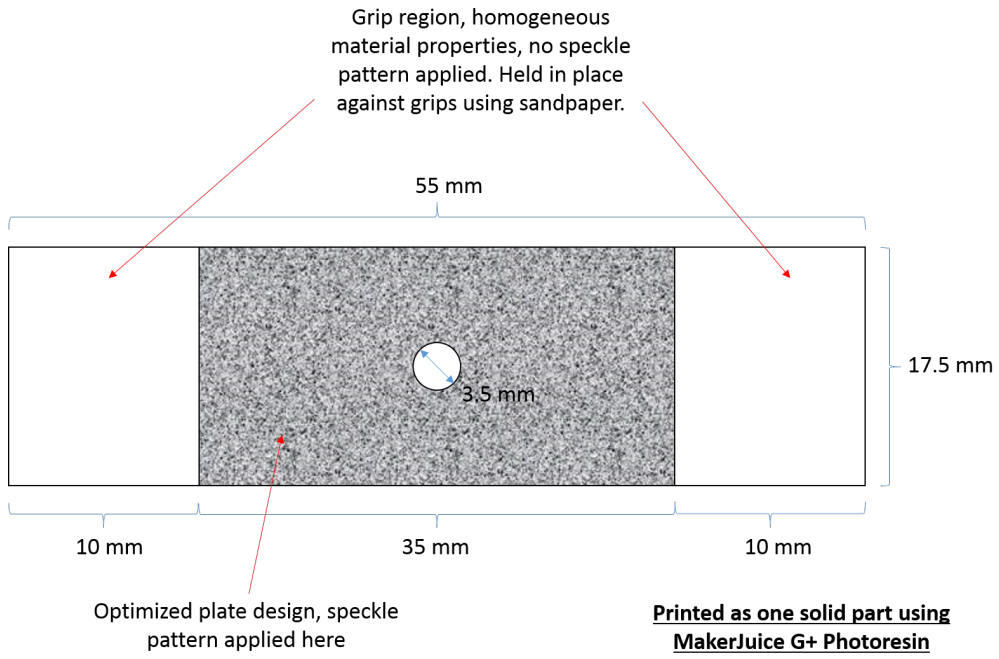

Figure 6.5: Specimen dimensions

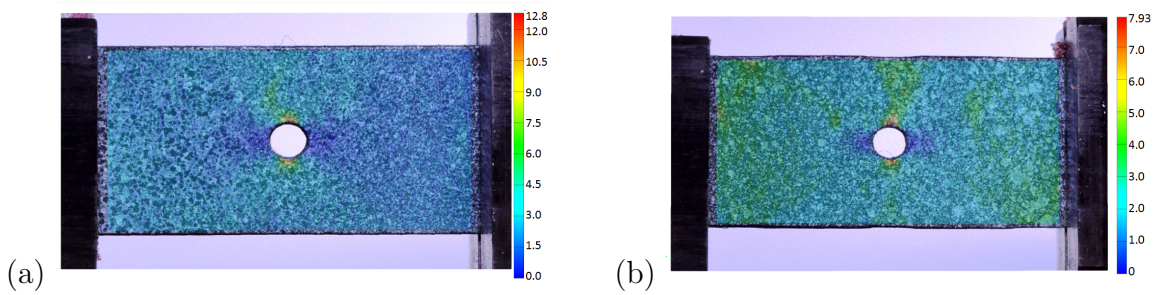

Figure 6.6: DIC results of strain fields just before failure for (a) homogeneous plate (b) optimized plate.

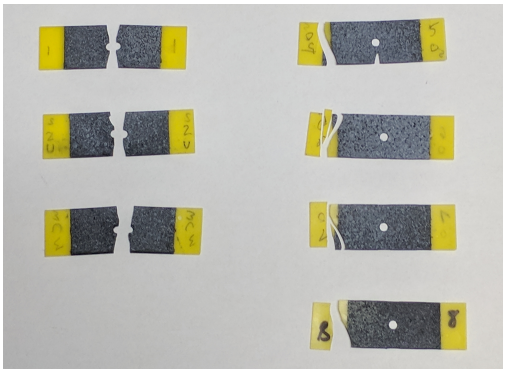

Figure 6.7: Failure modes of tested specimens, plates on left are homogeneous, on right is the optimized design.

distributed strain field, and the pattern qualitatively resembles the strain field calculated by the finite element analysis. Optimized plates also failed differently than homogeneous plates; all homogeneous plates failed near the hole, as expected, but the optimized plates consistently failed away from the hole and closer to the grip region instead, as seen in Figure 6.7. This is likely due to the milder strain gradients in the optimized plates coupled with lower strengths in the region of failure. Global Young's modulus for both designs were equivalent, as expected; values for representative samples are shown in Table 6.1.

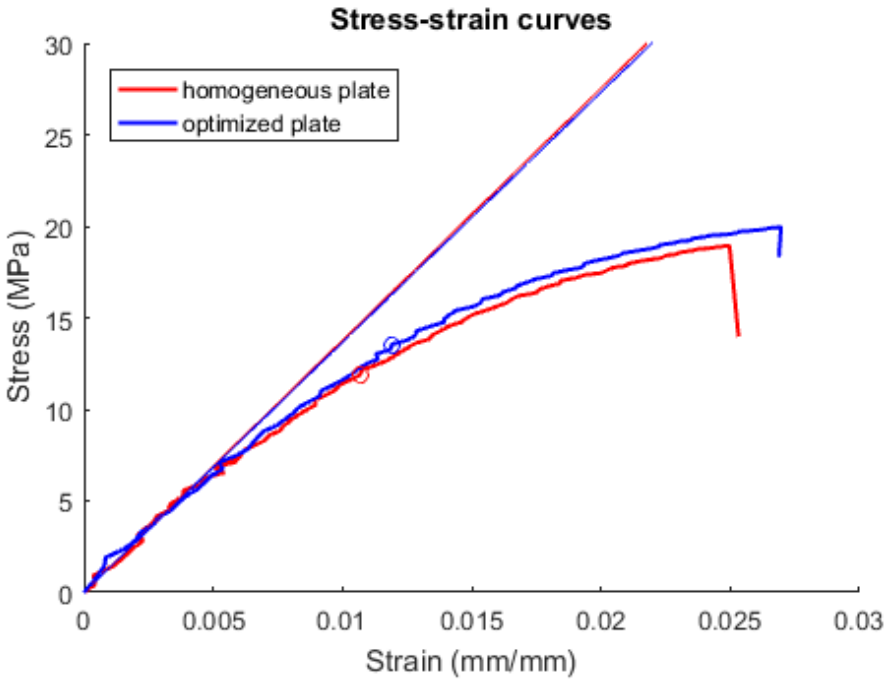

Figure 6.8: Stress-strain curves of representative plate samples tested in tension.

Table 6.1: Tensile data of representative samples.

	Global Young's modulus (MPa)	Ultimate strength (MPa)	Yield strength (MPa)	Strain at fracture (mm/mm)
homogeneous plate	1377	18.94	11.89	0.0253
optimized plate	1366	19.94	13.54	0.0270

Chapter 7

MULTI-OBJECTIVE FUNCTION

Creating a design optimized to minimize strain energy gradients was proven to be successful at reducing the structural impact of geometric discontinuities; however, this method introduces an unexpected weakness elsewhere in the plate if strength changes are not also taken into consideration. Recall that light intensity not only changes Young's modulus but also strength, so regions with low modulus also exhibit low strength, which was not accounted for in the original formulation. Using that original formulation, gradients in the plate are minimized and redistributed, but even this mild shift in strain distribution can lead to failure when combined with lowered strength in the same zone, as can be seen in Figure 7.1. As a results, the plates optimized only for strain energy gradients are not significantly stronger than a homogeneous plate. Though strength changes were not taken into consideration in the original model, by integrating failure analysis and changes in strength into the model, it should be possible to not only design a part with reduced strain energy gradients, but that can withstand greater loads as well.

7.1 Second objective function

In order to find a design that exhibits higher overall strength, it is necessary to define a second objective function that seeks to maximize the load the plate can withstand. This can be done by checking the margin to failure in each element at each iteration, and maximizing the minimum margin it in the optimization process. First, one must find the corresponding yield strength, Y, that will result from the digital grayscale value needed to produce the desired Young's modulus in each element, using strength data gathered by experiments.

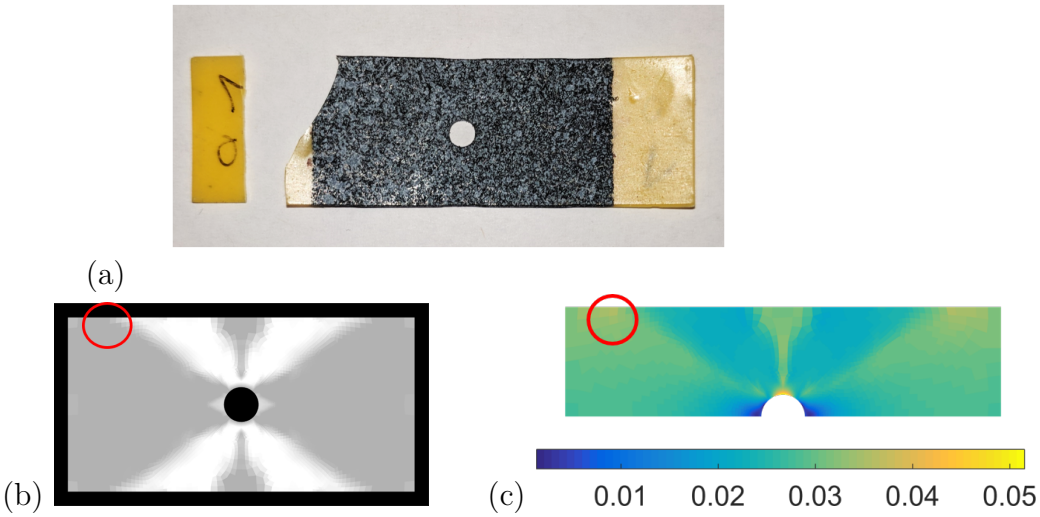

Figure 7.1: Point of failure in (a) failed specimen corresponds to (b) low light intensity in grayscale image used in 3D printing process and (c) high relative strain in the same zone.

Then, assuming von Mises failure criteria, calculate the von Mises stress in each element, σ_v^e, and find the margin to failure by $M^e = Y^e - \sigma_v^e$. The element closest to failure is of concern, and so the objective function targets the element with the smallest margin by defining the objective function as $S = \min(M^e)$. The optimization model then is to maximize S, as seen in Equation 7.1, in order to find a design that can has a greater margin to failure, and therefore can better withstand a greater load.

$$\begin{aligned} \max_{E} \quad & S(E) \\ & S(E) = \min M^e \\ \text{s.t.} \quad & 0.9 \leq E \leq 1.5GPa \end{aligned} \tag{7.1}$$

7.2 Multi-objective function formulation

Two objective functions have now been established for this project, one that seeks to minimize strain energy gradients (Equation 3.7), and another to maximize the load that can be withstood by the new design (Equation 7.1). There are a few established methods that exist for formulating optimization problems with multiple objective functions, three that are discussed here are goal programming, pre-emptive goal programming, and weighted sum.

In goal programming, the aim is to reach desired target levels, with emphasis placed on exceeding them as much as possible. There can be a lower, one sided goal, which sets a lower limit on acceptable values and aims to exceed it as much as possible. Another possibility is an upper, one sided goal, which sets an upper limit that cannot be exceeded, and aims to fall under this goal by as much as possible. Two-sided goals can also be used if the goal is a specific value that should met exactly. Goal programming also has the potential to use soft or hard constraints depending on if said constraint is preferred or required. Pre-emptive goal programming is a variation of goal programming in which some goals are considered significantly more important than others. In this method, first the most important objective function is maximized or minimized, then the second most important one is maximized or minimized, and so on. More information on these methods can be found in literature by Hillier and Lieberman as well as Rardin [35, 36].

For application to this project, both objective functions are of about equal importance, and the constraints to Young's modulus are hard constraints, as exceeding this range is not possible using this method of 3D printing. One possible goal that could be used in goal programming could be to improve G and S compared to an equivalent homogeneous plate. However, what would be considered an equivalent homogeneous design would change each iteration, so there is no fixed value from which to compare G or S. Not allowing a design to fail ($S > 0$) could also be considered a goal, but since the applied load to the plate is fixed at an arbitrary value, $S = 0$ may not necessarily correspond to a lower limit for a homogeneous

plate, therefore exceeding zero may not necessarily correspond to an improved design.

Because the objective is to strictly increase S and decrease G with no further specific goals to be achieved, it is best to directly minimize and maximize the desired objective functions. Weighted sum is a suitable method of multi-objective formulation in a case such as this. Weighted sum method aims to directly and simultaneously maximize and/or minimize desired quantities, and uses weights to determine importance of each objective function. General formulation for weighted sum method is shown in Equation 7.2, where n is the number of objective functions, $r_i(x)$ are the objective functions, and W_i are corresponding weights.

$$f(x) = \sum_{i=1}^{n} W_i * r_i(x) \tag{7.2}$$

Applied to this problem, both objective functions are of about equal importance, so weights must be adjusted to reflect this. The weight corresponding to strain energy gradient should be positive since it is to be minimized, and the weight corresponding to margin to failure should be negative since it is to be maximized. After some sample preliminary runs, it was observed that S tended to converge to a larger value than G. Finite element analysis and objective function evaluation was performed for a homogeneous plate, and the ratio of the values of G to S was calculated to have a ratio of G to S of about 14.5. This value is proposed as a preliminary value for the weight on G in order to balance the importance of each objective function, where the weight on S is -1. The resulting optimization formulation is shown in Equation 7.3. Depending on the resulting design, it may be necessary to adjust weights in order to study the efficient frontier and determine the relative desired importance and sensitivity of each objective function.

$$
\begin{aligned}
\min_{E} \quad & f(E) \\
& f(E) = 14.5 * G(E) - S(E) \\
& G(E) = \max ||\nabla W^e|| \\
& S(E) = \min M^e \\
\text{s.t.} \quad & 0.9 \leq E \leq 1.5 \ GPa
\end{aligned}
\tag{7.3}
$$

Chapter 8

CONCLUSION

8.1 Future work

8.1.1 Optimization improvements

It has become evident that it is necessary not only to account for changes in Young's modulus, but also strength in order to prevent undesired weaknesses to the design. Two objective functions to account for strain energy gradients as well as strength changes have been formulated, and methods for combining both functions have been discussed. Future work includes studying the efficient frontier of the two objective functions and establishing a new design. This design will then be 3D printed and tested to verify if an improved strength is achieved, as well as a different failure mode than a homogeneous plate.

The sequential quadratic programming method used by fmincon was shown to be an effective optimization algorithm for this problem compared to other methods investigated, but other algorithms may be more computationally efficient. Integration of HASPLID with SQP may yield a faster convergence to the optimum than HASPLID with stochastic search, as well as more reliable convergence to optimum for nonconvex problems. Though Response Surface was proven to be ineffective for this problem, other meta modeling methods may prove to be more well suited for this problem. Future work may include investigating these and other optimization algorithms in order to find an even more efficient and well suited algorithm for this problem.

8.1.2 Other applications

This work explores the effect of heterogeneous design on static loads in particular, but there is also potential to use heterogeneous design to account for other types of loads, such as thermal and dynamic loads. Additionally, this study has primarily focused on developing a design method that is compatible with additive manufacturing of heterogeneous parts using vat photopolymerization, but this method can be applied to other manufacturing technologies. Specifically, there is potential to apply this design method to objects printed with polyjet 3D printing, however, many commercially available polyjet printers can only print discrete ratios of polymers. Therefore, design using this method will require implementation of discrete optimization rather than continuous. It may also be possible to use FDM with graphene/polymer nanocomposites for heterogeneous design, so future work may include research into methods of distributing nanoparticle concentrations in a controlled matter throughout filament used in this process. Additive manufacturing is a quickly growing field, and as research is developed into other functionally graded material processes, this design method may be applicable to such methods in the future.

8.2 Accomplishments & findings

As new additive manufacturing technology has enabled the production of heterogeneous materials, it is now imperative to develop methods for finding optimal designs that use this to the greatest possible structural benefit. Of these technologies, the specific 3D printing method investigated for application to this study can spatially vary crosslink density in photoresins to control Young's modulus and strength, while keeping other material properties invariant. A method for structurally optimal design of heterogeneous materials has been developed, and used to create an optimized plate with a hole that can be printed using vat photopolymerization. Finite element results of this design show clear improvements to stress, strain, and strain energy distributions, which have been validated with experiments.

Experiments also show that optimized plates exhibit consistently different failure modes than homogeneous plates, indicating successful reduction of the structural impact of the hole. Implications of this study include increased flexibility when designing parts that require geometric discontinuities, such as bolt holes. Through the use of 3D printing technologies and optimization of the material properties using the design method proposed in this study, design engineers would be able to design around discontinuities without increasing mass or making further undesired changes to geometry.

BIBLIOGRAPHY

[1] Jonathan Glancey. The crashes that changed plane design forever. *British Broadcasting Corporation*, April 2014.

[2] Federal Aviation Administration. de havilland dh-106 comet 1. *Lessons Learned from Civil Aviation Accidents*.

[3] Gregory I. Peterson, Johanna J. Schwartz, Di Zhang, Benjamin M. Weiss, Mark A. Ganter, Duane W. Storti, and Andrew J. Boydston. Production of materials with spatially-controlled cross-link density via vat photopolymerization. *ACS Applied Materials & Interfaces*, 8(24):29037–9043, 2016.

[4] Hideo Kodama. Automatic method for fabricating a three-dimensional plastic model with photo-hardening polymer. *Review of Scientific Instruments*, 52(11):1770–3, 1981.

[5] Charles W Hull. *Apparatus for Production of Three-Dimensional Objects By Stereolithography*. Number 4575330. March 1986.

[6] S. Scott Crump. *Apparatus and method for creating three-dimensional objects*. Number 5121329. June 1992.

[7] Filemon Schoffer. How expiring patents are ushering the next generation of 3d printing. *Tech Crunch*, May 2016.

[8] John Hornick and Dan Roland. Many 3d printing patents are expiring soon. *3D Printing Industry*, December 2013.

[9] Fredrick R. Ishengoma and Adam B. Mtaho. 3D Printing: Developing Countries Perspectives. *International Journal of Computer Applications*, 104(11):30–34, 2014.

[10] Joshua M. Pearce, Christine Morris Blair, Kristen J. Laciak, Rob Andrews, Amir Nosrat, and Ivana Zelenika-Zovko. 3-D Printing of Open Source Appropriate Technologies for Self-Directed Sustainable Development. *Journal of Sustainable Development*, 3(4):17–29, 2010.

[11] John L Irwin. The RepRap 3-D Printer Revolution in STEM Education. *2015 ASEE Annual Conference & Exposition*, June 2014.

[12] David H. Freedman. Layer by layer. *MIT Technology Review*, December 2011.

[13] James O. Hardin, Thomas J. Ober, Alexander D. Valentine, and Jennifer A. Lewis. Microfluidic printheads for multimaterial 3d printing of viscoelastic inks. *Advanced Materials*, 27(21):3279–3284, 2015.

[14] Pia Taupert. *Continuously-variable material properties in RepRap 3D printing.* Master's thesis, University of Bath, Bath, UK, 2012.

[15] Jeffrey Scott Raquet. *An investigation into the material properties and precision of rapid prototyping technology.* PhD thesis, University of North Carolina at Charlotte, Charlotte, NC, 2005.

[16] Frank Filisko, Doris Filisko, Kaajal Raj Juggernauth, and Anthony Waas. *Dispersion Method For Particles in Nanocomposites and Method of Forming Nanocomposites.* Number 20110064940A1. March 2011.

[17] Dimitri Kokkinis, Manuel Schaffner, and André R. Studart. Multimaterial magnetically assisted 3D printing of composite materials. *Nature Communications*, 6, 2015.

[18] Jeffrey R. Potts, Daniel R. Dreyer, Christopher W. Bielawski, and Rodney S. Ruoff. Graphene-based polymer nanocomposites. *Polymer*, 52(1):5–25, 2011.

[19] Zelda B. Zabinsky. Random search algorithms. *Wiley Encyclopedia of Operations Research and Management Science*, 8, 2011.

[20] Zelda B. Zabinsky, David Bulger, and Charoenchai Khompatraporn. Stopping and restarting strategy for stochastic sequential search in global optimization. *Journal of Global Optimization*, 46(2):273–286, 2010.

[21] G. E. P. Box and K. B. Wilson. On the experimental attainment of optimum conditions. *Journal of the Royal Statistical Society. Series B (Methodological)*, 13(1):1–45, 1951.

[22] Robert B Wilson. *A simplicial algorithm for concave programming*. PhD thesis, Harvard University, 1965.

[23] Roger Fletcher. Methods for Nonlinear Constraints. In *NATO Advanced Research Institute on Nonlinear Optimization*, pages 481–492, Cambridge, 1981.

[24] Jorge Nocedal and Stephen J Wright. *Numerical Optimization*. Springer, 1999.

[25] Ashok D. Belegundu and Tirupathi R. Chandrupatla. *Optimization Concepts and Applications in Engineering*. Prentice Hall, Upper Saddle River, New Jersey, 2011.

[26] Roger Fletcher. *Practical Methods of Optimization*. Chichester, 2 edition, 1987.

[27] William Karush. *Minima of Function of Several Variables with Inequalities as Side Conditions*. PhD thesis, University of Chicago, Chicago, IL, 1939.

[28] Harold W. Kuhn and Albert W. Tucker. Nonlinear Programming. In *Second Berkeley Symposium*, pages 481–492, 1951.

[29] A.J.M. Ferreira. *MATLAB Codes for Finite Element Analysis: Solids and Structures*. Dordrecht, Springer, Netherlands, 2009.

[30] D. H. Ackley. *A connectionist machine for genetic hillclimbing*. Kluwer Academic Publishers, 1987.

[31] User: Gaortizg. Ackley function. *Wikimedia Commons / Creative Commons Attribution-Share Alike 3.0 Unported / https://creativecommons.org/licenses/by-sa/3.0/*, April 2012.

[32] Zelda B. Zabinsky. *Stochastic Adaptive Search for Global Optimization*. Kluwer Academic Publishers, 2003.

[33] Makerjuice g+ hard multi-purpose resin. *MakerJuice Labs*, 2016.

[34] *D638-14 Standard Test Method for Tensile Properties of Plastics*. ASTM International, West Conshohocken, PA, 2014.

[35] Frederick S. Hillier and Gerald J. Lieberman. *Introduction to Operations Research*. Mcgraw Hill Education, 2015.

[36] Ronald L. Rardin. *Optimization in Operations Research*. Prentice Hall, 1998.